



Generalized phase profile design method for tunable devices using bilayer metasurfaces

XIAOYU CHE,¹ RUI GAO,¹ YEFENG YU,¹  WEIJIAN LIU,¹ YIFENG SUN,¹ DAN ZHU,¹ WENYOU QIAO,¹ LINGJIE WANG,² JIANPING ZHANG,² QUN YUAN,^{1,3} AND ZHISHAN GAO^{1,4}

¹*School of Electronic and Optical Engineering, Nanjing University of Science and Technology, Nanjing 210094, China*

²*Key Laboratory of Optical System Advanced Manufacturing Technology, Changchun Institute of Optics, Fine Mechanics and Physics, Chinese Academy of Sciences, Changchun 130033, China*

³*karmen86913@gmail.com*

⁴*zhishan.gao@njust.edu.cn*

Abstract: Tunable devices based on bilayer metasurfaces have attracted researchers' attention in recent years for their accurate tuning abilities and high integration. In tunable devices such as tunable beam splitters and Alvarez metalenses, opposite quadratic or cubic target phase profiles are imparted on both layers, and a varying total phase profile arises through the relatively lateral displacement between the two layers. However, there is a lack of a generalized target phase profile design method to design these tunable devices. In this study, a generalized phase profile design method named Integral of Total Phase Profile Difference (ITPD) is proposed to calculate the target phase profiles of both layers. Multiple integral equations describe the relationship between the target phase profiles and the total phase profiles. Based on this method, a tunable beam splitter and an Alvarez metalens are redesigned respectively. Moreover, a new tunable device that can be converted from a beam splitter to a metalens is designed by the ITPD method. The ITPD design method is promising for designing tunable devices with arbitrary total phase profiles in dynamic or multifunctional optical systems.

© 2021 Optica Publishing Group under the terms of the [Optica Open Access Publishing Agreement](#)

1. Introduction

Active metasurfaces, whose optical properties can be changed after fabrication [1,2], can substitute the traditional optical lenses in the ultrathin dynamic optical equipment. Several means to design the active metasurfaces have been exploited with the help of flexible substrates [3], phase change materials [4,5] and bilayer metasurfaces based on the microelectromechanical systems (MEMS) [6,7]. Bilayer metasurfaces have much design freedom and the MEMS-based ones have advantages over the other active metasurfaces in phase control accuracy and simplicity. Among them, the bilayer metasurfaces with lateral displacement (BMLDs), where the total phase profile varies versus relatively lateral displacement between the two layers, can provide a larger tuning range than the bilayer metasurfaces with relatively longitudinal displacement [6] as well as higher transmission efficiency than the bilayer metasurfaces with mutual rotation [8].

An Alvarez lens design [9], capable of rapidly changing the focal length through the relatively lateral displacement between two separate lenses, has been introduced to metalens systems [10,11]. In the Alvarez metalens, the quadratic total phase profile can be decomposed into two cubic target phase profiles whose coefficients are opposite to each other. By laterally moving the metasurfaces with cubic phase profiles in the BMLDs, the coefficients of the quadratic total profile will slowly vary, which causes the continuous zoom [12]. The core idea of this tunable lens design is utilizing the cancellation of two same-order functions with opposite coefficients to get a lower-order function [13]. Relying on this principle, a tunable beam splitter was also achieved through the cancellation of two quadratic phase profiles to get a linear gradient phase

profile [7]. Nevertheless, the above designs only consider the target phase profiles with cubic or quadratic homogeneous functions, and there is a lack of a generalized phase profile design method that can calculate the target phase profiles in various tunable devices.

Inspired by the above designs, the total phase profile can be decomposed into two phase profiles as target phase profiles of the bilayer metasurfaces. Then integral of total phase profile difference (ITPD), a generalized phase profile design method, has been proposed to calculate the arbitrary target phase profiles in the tunable devices with arbitrary total phase profiles. In this method, a couple of integral equations are proposed to describe the relationship between the total phase profiles and the target phase profiles, also explaining the cancellation principle. The concrete target phase profile functions, not limited as homogeneous functions, can be clearly deduced from the integral equations when we know the two total phase profiles and the relative displacement value. To prove the generality of the ITPD method, the tunable beam splitter and the Alvarez metalens are redesigned respectively. Moreover, a new tunable device which can be converted from a beam splitter to a focal lens is designed by ITPD method. The ITPD design method is promised to be applied in tunable devices design in imaging and sensing optical systems.

2. Theory

2.1. ITPD design method

Inspired by the Alvarez lens design, the total phase profiles of the device can be decomposed into two target phase profiles. As shown in Figs. 1(a) and 1(b), we know the total phase profile before the lateral displacement ϕ_1 and the total phase profile after the lateral displacement ϕ_2 . Assuming that φ_1 and φ_2 denote the target phase profiles of the first metasurface (M1) and the second metasurface (M2), the relationship between the known total phase profiles and the unknown target phase profiles can be described by

$$\begin{cases} \varphi_1(x, y) + \varphi_2(x, y) = \phi_1 \\ \varphi_1(x + d, y) + \varphi_2(x - d, y) = \phi_2 \end{cases}, \quad (1)$$

where d represents the relatively lateral displacement. Then the difference of the two equations in Eq. (1) is written as

$$\frac{\varphi_1(x + d, y) - \varphi_1(x, y)}{d} - \frac{\varphi_2(x, y) - \varphi_2(x - d, y)}{d} = \frac{\phi_2 - \phi_1}{d}. \quad (2)$$

When the relatively lateral displacement d is small, Eq. (2) can be changed into

$$\frac{\partial \varphi_1(x, y)}{\partial x} - \frac{\partial \varphi_2(x, y)}{\partial x} = \frac{\phi_2 - \phi_1}{d}. \quad (3)$$

Note that both sides of Eq. (3) can be integrated, and then the equation can be rewritten as

$$\varphi_1 - \varphi_2 = \int \frac{\phi_2 - \phi_1}{d} dx. \quad (4)$$

Combing Eq. (4) with Eq. (1), phase profiles φ_1 and φ_2 can be derived separately with the known total phase profiles ϕ_1 and ϕ_2 by

$$\begin{cases} \varphi_1 = \frac{\phi_1}{2} + \frac{1}{2d} \int (\phi_2 - \phi_1) dx \\ \varphi_2 = \frac{\phi_1}{2} - \frac{1}{2d} \int (\phi_2 - \phi_1) dx \end{cases}. \quad (5)$$

The couple of integral equations have comprehensive application value in tunable devices.

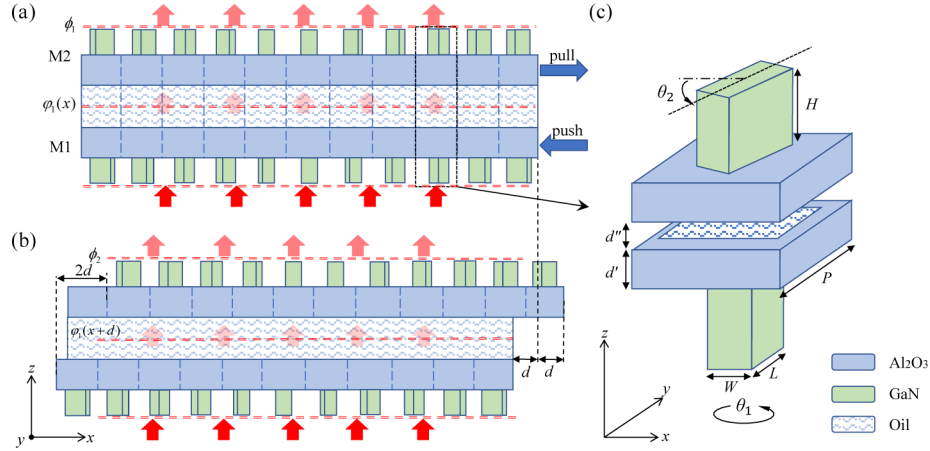


Fig. 1. The schematic diagram of the BMLDs. The side view of the bilayer geometric metasurfaces (a) before the lateral displacement and (b) after the lateral displacement. The M1 and the M2 are moved a lateral distance of d along the $-x$ -axis and $+x$ -axis directions. (c) The 3D view of the cascading unit structures in M1 and M2 with geometric parameters (W, L, H, d', d'', P) which are rotated θ_1 and θ_2 counterclockwise around the z -axis. The nanofins are made of GaN and the substrates are made of Al₂O₃, while the gap between two substrates is filled with index-matching oil.

2.2. Bilayer geometric metasurfaces

To prove the proposed ITPD design method, metasurface based on the Pancharatnam-Berry (PB) phase [14] is adopted for simulation without loss of generality, which can split incident light into two orthogonally polarized beams. The working principles of the bilayer geometric metasurfaces are elaborated as follows. Under the illumination of the normal incident circularly polarized light, an anisotropic nanofin can be regarded as a miniature wave plate, which has the complex transmission coefficients t_e and t_o along the long and short axis. When the nanofin is rotated counterclockwise around the z -axis with an angle θ , the transmitted light field can be described by the Jones matrix as

$$E = J(\theta)\hat{e} = \mathbf{R}(\theta) \begin{bmatrix} t_e & 0 \\ 0 & t_o \end{bmatrix} \mathbf{R}(-\theta)\hat{e} = \frac{t_e + t_o}{2} \begin{bmatrix} 1 & 0 \\ 0 & 1 \end{bmatrix} \hat{e} + \frac{t_e - t_o}{2} \begin{bmatrix} \cos 2\theta & \sin 2\theta \\ \sin 2\theta & -\cos 2\theta \end{bmatrix} \hat{e}, \quad (6)$$

where the $\mathbf{R}(\theta)$ is the rotation matrix, the -2θ represents the PB phase, and the complex vector $\hat{e} = [1 \ \sigma i]^T$ represents the polarization state of the electric field. The imaginary part $\sigma = 1$ represents right-handed circularly polarized (RHCP) light, while $\sigma = -1$ represents left-handed circularly polarized (LHCP) light. By rotating the nanofins, full 2π phase coverage can be achieved under the circularly polarized incidence. Assuming that t_{o1} and t_{e1} are the complex transmission coefficients of the nanofin in the M1, while t_{o2} and t_{e2} are the corresponding coefficients of the nanofin in the M2, the coefficients can be simplified as

$$t_{o1} + t_{e1} = T_1, \quad t_{o1} - t_{e1} = T_2, \quad t_{o2} + t_{e2} = T'_1, \quad t_{o2} - t_{e2} = T'_2. \quad (7)$$

When θ_2 and θ_1 denote the rotation angle of the cascading nanofins in M2 and M1 as marked in Fig. 1(c), the Jones matrix can be written as

$$\mathbf{J}(\theta_1, \theta_2) = \mathbf{J}(\theta_2)\mathbf{J}(\theta_1) = \frac{1}{4} \begin{bmatrix} T_1 T'_1 + T_2 T'_2 e^{j2(\theta_2 - \theta_1)} & T_2 T'_1 e^{j2\theta_1} + T_1 T'_2 e^{j2\theta_2} \\ T_2 T'_1 e^{-j2\theta_1} + T_1 T'_2 e^{-j2\theta_2} & T_1 T'_1 + T_2 T'_2 e^{j2(\theta_1 - \theta_2)} \end{bmatrix}. \quad (8)$$

Then the total transmitted field with the incident circularly polarized light can be decomposed into four parts [15], which can be written as

$$\mathbf{E} = \frac{T_1 T'_1}{4} \hat{\mathbf{e}}^* + \frac{T_2 T'_1}{4} e^{-j2\theta_1} \hat{\mathbf{e}} + \frac{T_1 T'_2}{4} e^{-j2\theta_2} \hat{\mathbf{e}} + \frac{T_2 T'_2}{4} e^{j2(\theta_2 - \theta_1)} \hat{\mathbf{e}}^*, \quad (9)$$

where the symbol * represents conjugation. This equation implies that the propagating light in the gap between the two layers becomes LHCP light when the RHCP light normally illuminates the M1. The propagating light changes back to RHCP light after being diffracted by the M2. In addition, if the polarization conversion efficiency is high enough, T_1 and T'_1 will be approximated as zero so that the transmitted field can be completely described by the last term in Eq. (9). Then the total phase shift, which is equal to the double of the angle difference $2(\theta_2 - \theta_1)$, is completely determined by the PB phases of metasurfaces. Moreover, the monochromatic light with any polarization state can be deemed as the superposition of two orthogonally polarized light such as LHCP and RHCP light [16,17]. Then the light with various polarization states would be split by the bilayer geometric metasurfaces into LHCP and RHCP light along different directions.

Although the ITPD design method is meaningful for the design of bilayer optical elements, the operation of simply decomposing the target phase profile into two separate phase profiles requires that the two cascading optical elements are very close to each other. Equation (8) and (9) only work under the condition that the gap between the two cascading nanofins $G = 2d' + d''$ is restricted to the half of the Talbot length $\lambda_T = 2P^2/\lambda$ [8]. Meanwhile, to meet the fabrication limitation and eliminate the near-field crosstalk between M1 and M2, the gap is usually larger than the multiple incident wavelength, which is always larger than the Talbot length ($G > \lambda_T$), and there are several works mentioned that when the gap is equal to multiple Talbot lengths, the decomposition method is still working [18,19]. However, the arrangement of nanofins shown in Fig. 1 is inaccessible in practical fabrication for the thickness of the substrate is usually on the order of microns or millimeters, which is much larger than the gap between the cascading nanofins. The solution to this problem is turning every metasurface over to get face-to-face bilayer metasurfaces with the substrates out of the gap, as performed in previous works [7,20]. The arrangement of nanofins shown in Fig. 1 is only used for the simulations to verify the effectiveness and generality of the ITPD method.

3. ITPD method for different tunable devices

3.1. ITPD method for a tunable beam splitter design

Tunable beam splitters can be realized using the BMLDs. Then the ITPD method can be applied in the design of the target phase profiles of the both layers. As shown in Fig. 2(a), the incident LHCP light will be deflected at an angle θ_{t1} before the lateral displacement, while the RHCP light will be deflected at an angle $-\theta_{t1}$. In the same way, the bilayer geometric metasurfaces can split the light into LHCP and RHCP light with $\pm\theta_{t2}$ angles after the lateral displacement, as shown in Fig. 2(d). Then the tunable beam splitters are achievable. To design such devices, the total phase profiles are written as

$$\phi_i = -kx \sin \theta_{ti}, \quad i = 1, 2, \quad (10)$$

where k is the wave vector. According to the ITPD method, Eq. (10) can be substituted into Eq. (5) to get the target phase profiles of M1 and M2

$$\begin{cases} \varphi_1 = \frac{k(\sin \theta_{t1} - \sin \theta_{t2})}{4d} x^2 - \frac{k \sin \theta_{t1}}{2} x \\ \varphi_2 = \frac{k(\sin \theta_{t2} - \sin \theta_{t1})}{4d} x^2 - \frac{k \sin \theta_{t1}}{2} x \end{cases}. \quad (11)$$

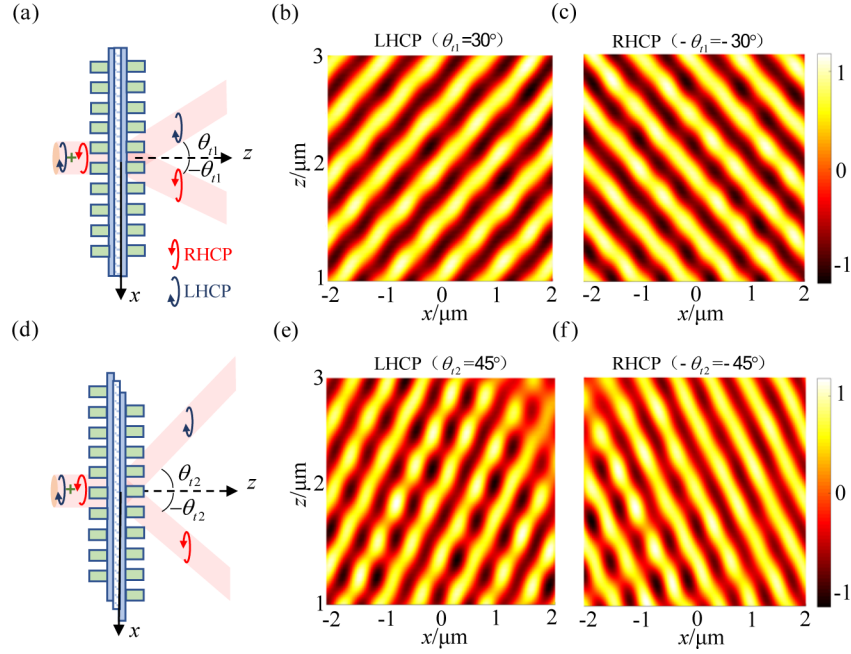


Fig. 2. The sketch of the tunable beam splitters based on the BMLDs (a) before the lateral displacement and (d) after the lateral displacement. The simulated real part of the split (b) LHCP and (c) RHCP electric field distribution under the normal incidence of LHCP and RHCP light in the xz -plane before the lateral displacement. The simulated real part of the split (e) LHCP and (f) RHCP electric field distribution under the normal incidence of LHCP and RHCP light in the xz -plane after the lateral displacement.

For comparison, the target phase profiles in the traditional design method [7], are listed as follows

$$\varphi'_1(x) = -\varphi'_2(x) = Ax^2. \quad (12)$$

The total phase profiles can be written as

$$\phi'_i = \varphi'_1(x + d_i) + \varphi'_2(x - d_i) = 4Ad_ix, \quad i = 1, 2, \quad (13)$$

and the deflection angles can be expressed as

$$\theta_{ii} = -\arcsin\left(\frac{4Ad_i}{k}\right), \quad i = 1, 2, \quad (14)$$

where the lateral displacement $d_2 - d_1 = d$. The constant A can be calculated by Eq. (14) with known deflection angles θ_{ii} and known lateral displacements d_i . If the constant A is decided, the target phase profiles φ'_i will be derived by Eq. (12) and the total phase profiles ϕ'_i will be derived by Eq. (13). The target phase profiles are expressed as quadratic homogeneous functions with opposite signs and, the total phase profiles are achieved by the superposition of the target phase profiles with different relatively lateral displacements. It can explain the cancelation principle that the superposition of two quadratic functions with opposite coefficients can get a linear function. The constant $A = k(\sin\theta_{11} - \sin\theta_{12})/4d$ can be derived by Eq. (14), and it can be found that $\varphi'_1(x + d_1)$ and $\varphi'_2(x - d_1)$ ignoring the constant terms are equal to φ_1 and φ_2 in Eq. (11) respectively. Compared with traditional method, Eq. (11) derived from ITPD describe the phase

profiles more directly without introducing the constant A . During the displacement, If the lateral displacement d_t is a variable on the section $[0, d]$, the split angle θ_t versus d_t can be described by

$$\sin \theta_t = (\sin \theta_{t2} - \sin \theta_{t1}) \frac{d_t}{d} + \sin \theta_{t1}. \quad (15)$$

Then the optical properties of the tunable beam splitter in the tuning process are clear.

Here, a tunable beam splitter is designed and simulated referring to the above theory. The θ_{t1} is set as 30° and the θ_{t2} is set as 45° . The lateral displacement d is set as $6 \mu\text{m}$ and the length of the linear aperture along the x -axis of the designed BMLDs is $60 \mu\text{m}$. As shown in Fig. 3(a), the simulated polarization conversion efficiency of the nanofin is close to 99% at 440 nm wavelength so that T_1 and T_1' are close to zero. Then the total phase shift is merely decided by double the difference of the rotation angles $2(\theta_2 - \theta_1)$ of cascading nanofins in M1 and M2. The involved gallium nitride (GaN) nanofin placed on alumina (Al_2O_3) substrate employs a cubic shape as shown in Fig. 1(c). The length L , width W , height H and period P are set as 170 nm, 60 nm, 600 nm, and 200 nm respectively as shown in the inset in Fig. 3(a). The selected nanofin has high transmittance in the visible waveband [21,22]. The gap between the two layers G is set as $1 \mu\text{m}$, and the refractive index matching oil has the same refractive index as Al_2O_3 at the wavelength of 440 nm. The simulations are implemented by the commercial electromagnetic simulation software (FDTD solutions, Lumerical Inc., Vancouver, Canada). The nanostructures' simulations are established by using perfect matching layer boundary conditions along each direction, while the linear arrays' simulations make a little difference that the boundary conditions along the y -axis direction are periodic. The nanofins in the M2 are standing on the $z = 0$ plane. As shown in Fig. 2(b), the simulated real part of the extracted LHCP electric field distribution in the xz -plane is calculated under the LHCP illumination before the lateral displacement, while the simulated real part of the extracted RHCP electric field distribution in the xz -plane is calculated under the RHCP illumination in Fig. 2(c). In the same way, the calculated real part of electric field distributions mentioned above after the lateral displacement are shown in Figs. 2(e) and 2(f). The slopes of the isopleth in Figs. 2(b) and 2(c) are approximate to ± 0.5 , which are equal to $\sin \pm 30^\circ$. Likewise, the slopes of the isopleths in Figs. 2(e) and 2(f) are about ± 1 , which are equal to $\sin \pm 45^\circ$. The theoretical target phase profiles and total phase profiles are shown in Figs. 3(b) and 3(c). During the displacement, the total phase profiles of both layers horizontally move along opposite directions and the total phase profile rotates clockwise in the x -phase plane. We also simulated the device at different lateral displacements, and the simulated split angles agree with the theoretical values calculated by Eq. (15) as shown in Fig. 3(d).

3.2. ITPD method for an Alvarez metalens design

One of the most important tunable devices that can be designed by the ITPD method is Alvarez metalens. Alvarez metalenses improve the space utility ratio, which is essential for various applications in mobile phones, robotics, endoscopes [23] and optical fibers lenses [24]. Assuming that f_1 and f_2 are in the focal length variation range as shown in Figs. 4(a) and 4(d), target phase profiles can be calculated by the ITPD method just enough. The target phase profiles of two wide-field imaging metalenses are described by the quadratic phase profiles [25–27]

$$\phi_i = -\frac{k(x^2 + y^2)}{2f_i}, \quad i = 1, 2, \quad (16)$$

Referring to the ITPD design method, Eq. (16) can be substituted into Eq. (5). Then the phase profiles φ_1 and φ_2 can be written as

$$\begin{cases} \varphi_1 = \frac{k}{12d} \left(\frac{1}{f_1} - \frac{1}{f_2} \right) x^3 + \frac{k}{4d} \left(\frac{1}{f_1} - \frac{1}{f_2} \right) xy^2 - \frac{k}{4f_1} (x^2 + y^2) \\ \varphi_2 = \frac{k}{12d} \left(\frac{1}{f_2} - \frac{1}{f_1} \right) x^3 + \frac{k}{4d} \left(\frac{1}{f_2} - \frac{1}{f_1} \right) xy^2 - \frac{k}{4f_1} (x^2 + y^2) \end{cases}, \quad (17)$$

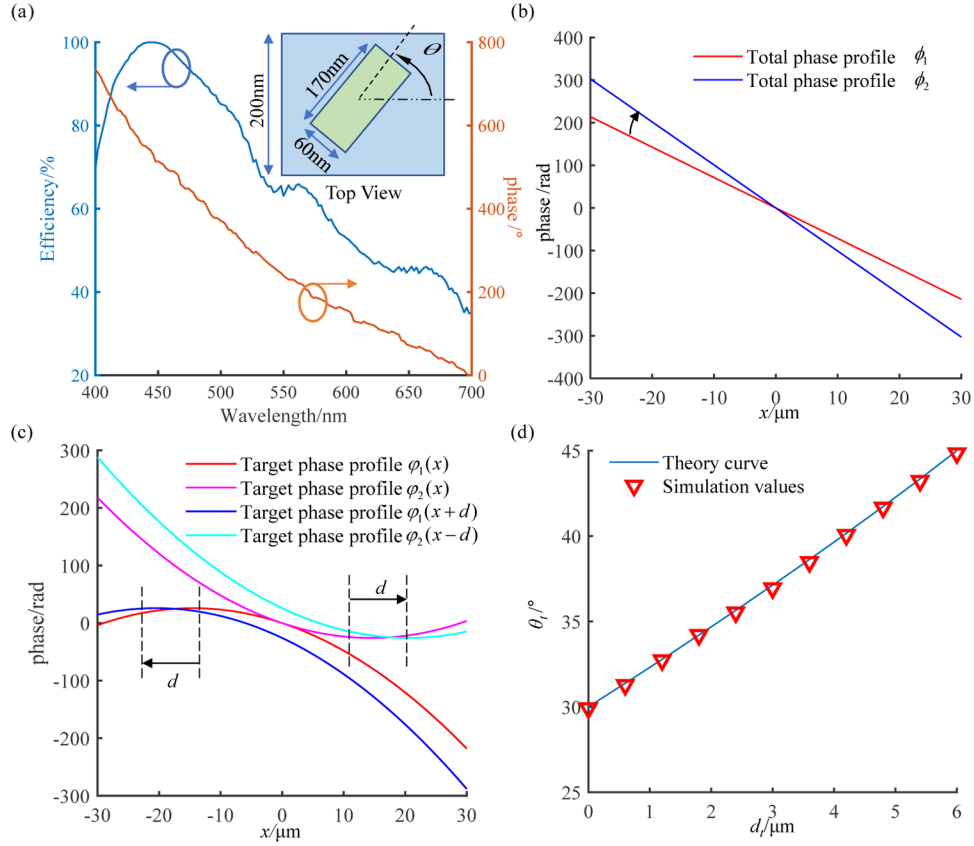


Fig. 3. (a) The properties of the selected nanofin ($W = 60$ nm, $L = 170$ nm, $H = 600$ nm, $P = 200$ nm). The phase response and polarization conversion efficiency of the selected nanofin change versus wavelength, and the inset shows the geometric parameters of the nanofin. The theoretical (b) target phase profiles and (c) total phase profiles when $d = 6$ μm , $\theta_{i1} = 30^\circ$, and $\theta_{i2} = 45^\circ$. The target phase profile horizontally moves and the gradient total phase profile rotates clockwise in the x -phase plane during the lateral displacement. (d) The theoretical and simulated split angle versus the lateral displacement d_i .

, where d is the lateral displacement. For comparison, the target phase profiles, which are expressed as cubic homogeneous with opposite coefficients in the traditional design method [11], are listed as follows

$$\varphi_1''(x, y) = -\varphi_2''(x, y) = -B\left(\frac{1}{3}x^3 + xy^2\right). \quad (18)$$

The total phase profiles are written as

$$\varphi_i'' = \varphi_1''(x + d_i, y) + \varphi_2''(x - d_i, y) = -2Bd_i(x^2 + y^2) - \frac{2}{3}Bd_i^3, \quad i = 1, 2, \quad (19)$$

and the focal lengths can be expressed as

$$f_i = \frac{k}{4Bd_i}, \quad i = 1, 2, \quad (20)$$

where the lateral displacement $d_2 - d_1 = d$, and B is a constant determining the zoom capability in essence. To seek the variation law of the focal length during the lateral displacement, we define

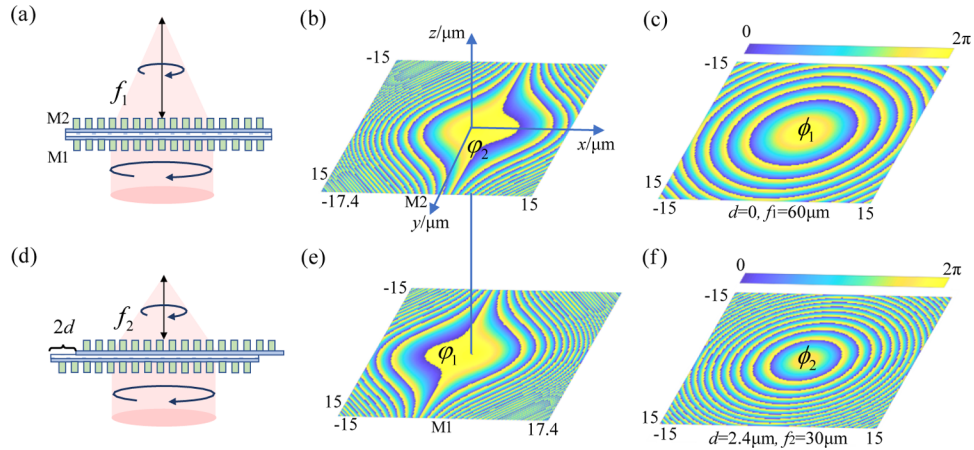


Fig. 4. The sketch of the Alvarez metalens illuminated by LHCP light (a) before and (d) after the lateral displacement. Theoretical target phase profiles of (b) M2 and (e) M1 are calculated by the ITPD method. The total phase profiles (c) ϕ_1 and (f) ϕ_2 are generated by the bilayer metasurfaces with the displacement $d = 0$ and $d = 2.4 \mu\text{m}$.

the lateral displacement d_t as a variable on the section $[0 d]$, the focal length f_t versus d_t can be described by

$$\frac{1}{f_t} = \frac{1}{f_1} - \left(\frac{1}{f_1} - \frac{1}{f_2} \right) \frac{d_t}{d}. \quad (21)$$

Equation (19) explains the cancelation principle that the superposition of two cubic functions with opposite coefficients can get a quadratic function. If constant B was fixed, the target phase profile φ_i'' would be derived by Eq. (18). Equation (20) implies that the focal length of the Alvarez metalens is in inverse proportion to the lateral displacement, by which the constant B can be derived as $B = k(1/f_2 - 1/f_1)/4d$. Compared with Eqs. (18–20) in traditional method, Eq. (17) derived from ITPD describe the phase profiles more directly without introducing the constant B .

To prove the accuracy of the equations derived from ITPD method, an Alvarez metalens with $f_1 = 60 \mu\text{m}$ and $f_2 = 30 \mu\text{m}$ has been designed. The effective aperture ranges $-15 \mu\text{m} < x < 15 \mu\text{m}$ and the lateral displacement d is set as $2.4 \mu\text{m}$. The geometric parameters of the selected nanostructure are the same as the parameters shown in the *section 3.1*. The diameter of the M1 is $32.4 \mu\text{m}$ (x ranges from $-17.4 \mu\text{m}$ to $15 \mu\text{m}$) and the diameter of the M2 is $32.4 \mu\text{m}$ (x ranges from $-15 \mu\text{m}$ to $17.4 \mu\text{m}$) as well so that both metasurfaces always fill in the effective aperture during the lateral displacement. As shown in Figs. 4(b) and 4(e), the target phase profiles of the M1 and M2 are calculated by Eq. (17), and then the total phase profiles are shown in Figs. 4(c) and 4(f). In addition, the numerical aperture ranges from 0.242 to 0.447.

The theoretical and simulated near-field phase profiles are shown in Fig. 5(a). The simulated ones have a little difference compared with the theoretical ones. The difference mainly comes from the variation of the phase profile propagating through the gap between the two layers. Then the wavefront from M1 will be out of shape when the light enters M2. Meanwhile, the light entering M2 is not a plane wave any more, which causes phase modulation inaccuracy of M2, and the resonances between nanofins with their neighbours also have an influence on the total phase profiles [28]. Finally, the actual simulated focal length is $55.8 \mu\text{m}$ before the lateral displacement, and the value changes to $27.5 \mu\text{m}$ after the lateral displacement. We also simulated the focal lengths when the lateral displacements d_t are $0.6 \mu\text{m}$, $1.2 \mu\text{m}$ and $1.8 \mu\text{m}$ as shown in Fig. 5(b).

Considering Eq. (1), the total phase profile ϕ_1 becomes zero when $\varphi_1 = -\varphi_2$. Then according to Eq. (2), the total phase profile ϕ_2 is only determined by the derivation of the target phase

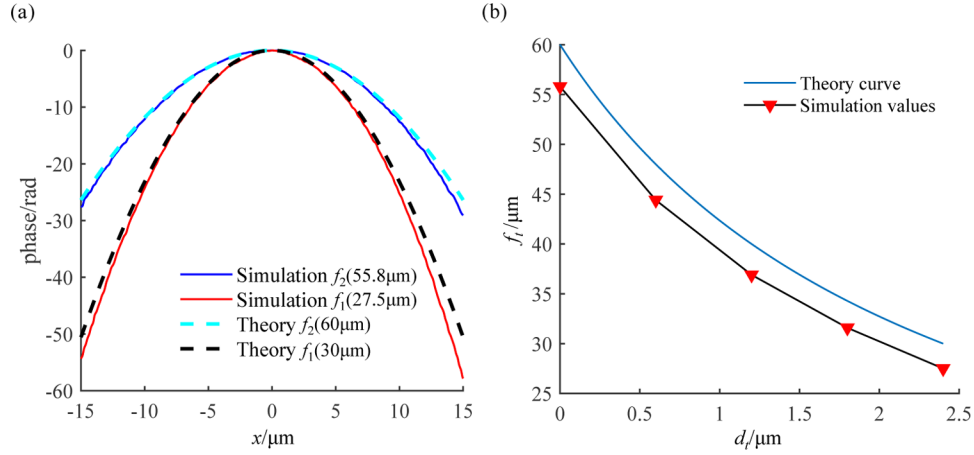


Fig. 5. (a) The simulated and theoretical near-field phase profiles of the center linear array of the BMLDs on the x -axis. (b) The simulated focal lengths (red) generated by the bilayer metasurfaces with the displacements $d_t = 0, 0.6 \mu\text{m}, 1.2 \mu\text{m}, 1.8 \mu\text{m},$ and $2.4 \mu\text{m}$. The theoretical focal length (blue) varies versus the lateral displacement.

profiles $\partial\varphi_i/\partial x$ and the relatively lateral displacement d . So far, the cancelation principle that the superposition of two same-order functions with opposite coefficients can get a lower-order function has been well explained by the ITPD method based on Eq. (2).

3.3. ITPD method for a multifunctional tunable device

In principle, The ITPD design method can be used for the design of target phase profiles of two layers in BMLDs. Assuming that the BMLDs can convert a linear total phase profile to a quadratic total phase profile, the total phase profiles can be written as

$$\begin{cases} \phi_1 = -kx \sin \theta \\ \phi_2 = -\frac{k(x^2+y^2)}{2f} \end{cases} \quad (22)$$

Then a new tunable device is designed. As shown in Figs. 6(a) and 6(d), the device before the relatively lateral displacement is used as a beam splitter with splitting angles $\pm \theta$ under the normal illumination of x -linear polarized (XLP) light, while the device after the lateral displacement is used as a metalens which has a focal length f . The target phase profiles can be derived by the ITPD method by substituting Eq. (22) into Eq. (5) as follows

$$\begin{cases} \varphi_1 = -\frac{kx^3}{12df} - \frac{kxy^2}{4df} + \frac{k \sin \theta x^2}{4d} - \frac{k \sin \theta x}{2} \\ \varphi_2 = \frac{kx^3}{12df} + \frac{kxy^2}{4df} - \frac{k \sin \theta x^2}{4d} - \frac{k \sin \theta x}{2} \end{cases}, \quad (23)$$

and the total phase profile during the lateral displacement can be accurately calculated by

$$\phi_t = \varphi_1(x + d_t) + \varphi_2(x - d_t) = -\frac{k}{2f} \frac{d_t}{d} (x^2 + y^2) - kx \sin \theta \left(1 - \frac{d_t}{d}\right) - \frac{k}{6f} \frac{d_t^3}{d}, \quad (24)$$

where the lateral displacement d_t is a variable on the section $[0, d]$. Equation (24) can be seen as the product of a metasurface with quadratic phase profile translating a linear phase, and the effect of oblique incidence is a spatial translation of the focal spot [25]. The equivalent focal

length is defined as $f_t = fd/d_t$, and the equivalent angle of the oblique incidence can be defined as $\theta_t = \arcsin(\sin\theta(1-d_t/d))$, so

$$\begin{aligned}\phi_t &= -\frac{k(x^2 + y^2)}{2f_t} - kx \sin \theta_t - \frac{kd_t^2}{6f_t} \\ &= -\frac{k}{2f_t}[(x + f_t \sin \theta_t)^2 + y^2] + \frac{f_t k \sin^2 \theta_t}{2} - \frac{kd_t^2}{6f_t}.\end{aligned}\quad (25)$$

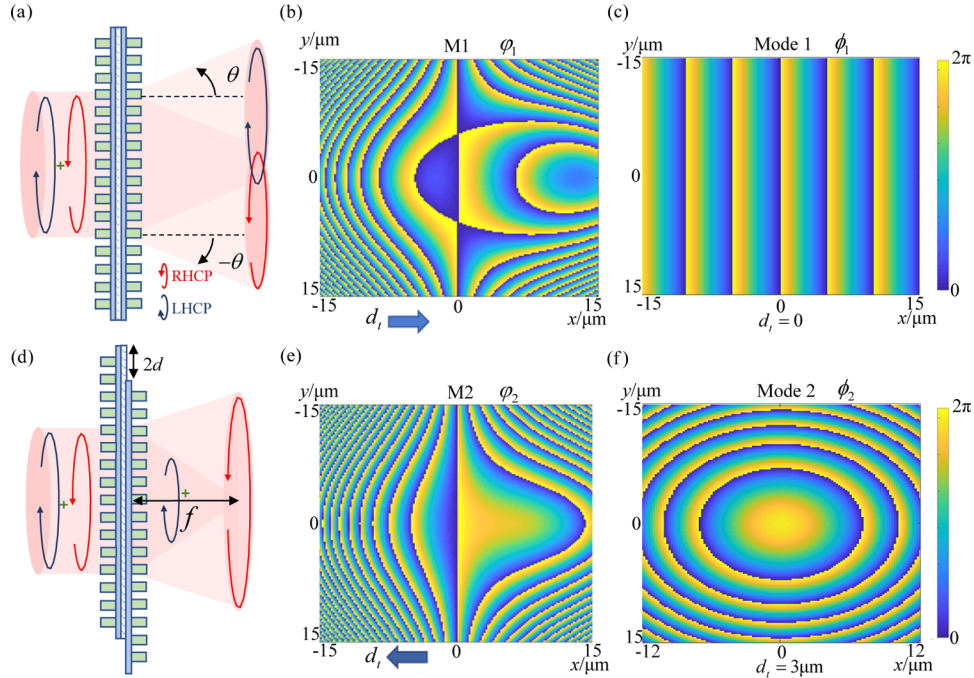


Fig. 6. The sketch of the tunable device (a) before and (d) after the relatively lateral displacement. (b) The theoretical target phase profile of the M1 and (e) that of M2 calculated by the ITPD method under the incident LHCP light. The theoretical total phase profiles (c) before and (f) after the displacement under the illumination of LHCP light.

The focal spot's coordinate in the xz -plane is $x = -f_t \sin \theta_t$ and $z = f_t$. It can be found that there is a linear relationship between z - and x -coordinate during the lateral displacement. If $d_t \rightarrow 0$, the equivalent focal length $f_t \rightarrow \infty$, and then the tunable device is converted from a metalens to a beam splitter.

Here, A tunable device with $f = 60 \mu\text{m}$ and $\theta = 5^\circ$ is designed. The gap and the nanofins' geometric parameters are the same as the ones in *section 3.1*. The effective linear aperture along the x -axis ranges from $-12 \mu\text{m}$ to $12 \mu\text{m}$, and the lateral displacement d is set as $3 \mu\text{m}$. We design the BMLDs on the section $-15 \mu\text{m} \sim 15 \mu\text{m}$ so that the both metasurfaces can fill in the whole effective aperture during the displacement. The theoretical target phase profiles of the M1 and the M2 calculated by the ITPD method with a $30 \mu\text{m} \times 30 \mu\text{m}$ aperture are shown in Figs. 6(b) and 6(e), and the total phase profiles before and after the lateral displacement are shown in Figs. 6(c) and 6(f) when a LHCP beam is used as the illumination.

Before the displacement, the simulated real parts of the transmitted LHCP and RHCP light electric fields are shown as fringe patterns in Figs. 7(a) and 7(b). The black dotted lines approximately denote the isopleths which represent the wavefronts of LHCP and RHCP light. The

deflection angle of LHCP light is around 4.97° and that of RHCP light is around -5.06° . During the displacement, the transmitted LHCP component converges at a spot, and the transmitted RHCP component is divergent, as shown in Figs. 8(a) and 8(d). To seek the variation law of focusing during the lateral displacement, we simulated the light intensity distributions in the xz -plane when the lateral displacements are $1\ \mu\text{m}$, $1.5\ \mu\text{m}$, $2\ \mu\text{m}$, $2.5\ \mu\text{m}$, and $3\ \mu\text{m}$ as shown in

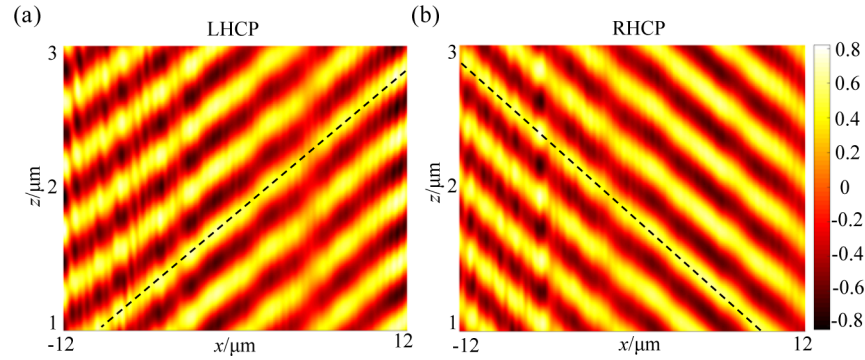


Fig. 7. The simulated real parts of the extracted transmitted (a) LHCP and (b) RHCP electric field distributions in the xz -plane under the normal XLP incidence.

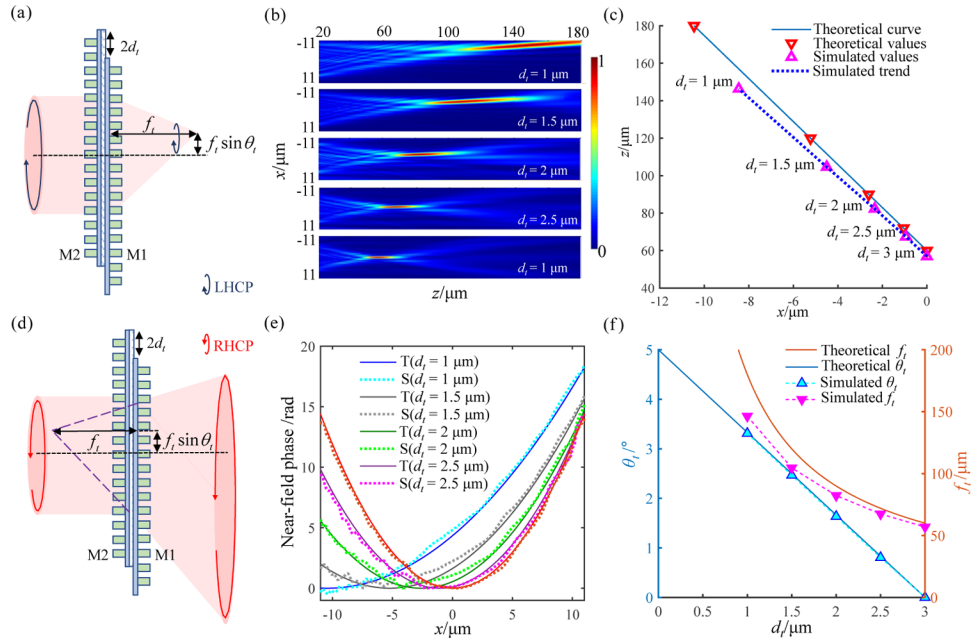


Fig. 8. The tunable device under the normal illumination of (a) the LHCP light and (d) the RHCP light during the lateral displacement. (b) The light intensity distributions of transmitted LHCP component in the xz -plane and (e) the near-field phase profile generated by the transmitted RHCP component under the XLP incidence when the lateral displacements $d_t = 1\ \mu\text{m}$, $1.5\ \mu\text{m}$, $2\ \mu\text{m}$, $2.5\ \mu\text{m}$, and $3\ \mu\text{m}$. ‘T’ means theory values while ‘S’ means simulation values. (c) The focal spot in the xz -plane moves versus the lateral displacement d_t . Theoretical values (red) and simulated values (violet) from left to right correspond to the lateral displacements $d_t = 1\ \mu\text{m}$, $1.5\ \mu\text{m}$, $2\ \mu\text{m}$, $2.5\ \mu\text{m}$, and $3\ \mu\text{m}$. (f) The theoretical and simulated f_t (red) and θ_t (blue) are tuned versus the lateral displacement d_t .

Fig. 8(b). The focus spots extracted from the light intensity distributions are shown in Fig. 8(c). It can be also found that the focal spot moves along a straight line in the xz -plane during the lateral displacement, and the slope of the line is equal to $-\csc\theta_l$. The near-field phase profiles which cause divergent wavefronts are generated by the transmitted RHCP light as shown in Fig. 8(e). The equivalent focal length and oblique incidence angle vary versus the displacement d_l as shown in Fig. 8(f). The reasons for the differences between the simulated and theoretical focal length are the same as those in the Alvarez metalens design.

In addition, the use of geometric metasurfaces is to split light. If we only need beam deflection instead of beam splitting, geometric metasurfaces can be replaced by other kinds of metasurfaces. Furthermore, the target phase profiles or total phase profiles can be expressed as arbitrary functions, which can generate free-form wavefronts. As we know, the XY polynomial is used for the characterization of free-form surfaces, so ϕ_1 and ϕ_2 in Eq. (5) are permitted as functions containing XY polynomials without loss of generality. Then the phase profiles φ_1 and φ_2 can be achieved to design the tunable devices based on BMLDs which can switch between two free-form phase profiles. We believe that the ITPD will be helpful for many multifunctional devices design.

4. Conclusions

In this research, the ITPD design method has been proposed to design tunable devices whose total phase profile can be tuned through relatively lateral displacement. Different from the traditional design method, the ITPD method gives a couple of generalized integral equations to describe the relationship between the target phase profiles and the total phase profiles, which has wider applications for tunable devices. A tunable beam splitter and an Alvarez metalens are redesigned by the ITPD method to approve its generality. A new tunable device, which can be converted from a beam splitter to a metalens whose focal spot moves along an oblique line for LHCP light, is designed using the ITPD method. This generalized method is anticipated to design doublet free-form surfaces in complex beam steering systems and expand enormous functions of ultrathin devices.

Funding. National Key Research and Development Program of China (2019YFB2005500); National Natural Science Foundation of China (62175107, U1931120); Six Talent Peaks Project in Jiangsu Province (RJFW-019); Foundation of key laboratory of optical system advanced manufacturing technology, Chinese academy of sciences (KLOMT190201).

Disclosures. The authors declare no conflicts of interest.

Data availability. The data that support the plots within this paper are available from the corresponding authors upon reasonable request.

References

1. S. Sun, Q. He, J. Hao, S. Xiao, and L. Zhou, "Electromagnetic metasurfaces: physics and applications," *Adv. Opt. Photonics* **11**(2), 380–479 (2019).
2. L. Kang, R. P. Jenkins, and D. H. Werner, "Recent Progress in Active Optical Metasurfaces," *Adv. Opt. Mater.* **7**(14), 1801813 (2019).
3. H. Ee and R. Agarwal, "Tunable Metasurface and Flat Optical Zoom Lens on a Stretchable Substrate," *Nano Lett.* **16**(4), 2818–2823 (2016).
4. X. Yin, T. Steinle, L. Huang, T. Taubner, M. Wutting, T. Zentgraf, and H. Giessen, "Beam switching and bifocal zoom lensing using active plasmonic metasurfaces," *Light Sci. Appl.* **6**(7), e17016 (2017).
5. M. Y. Shalaginov, S. An, Y. Zhang, F. Yang, P. Su, V. Liberman, J. B. Chou, C. M. Roberts, M. Kang, C. Rios, Q. Du, C. Fowler, A. Agarwal, K. A. Richardson, C. R. Baleine, H. Zhang, J. Hu, and T. Gu, "Reconfigurable all-dielectric metalens with diffraction-limited performance," *Nat. Commun.* **12**(1), 1225 (2021).
6. E. Arbabi, A. Arbabi, S. M. Kamali, Y. Horie, M. Faraji-Dana, and A. Faraon, "MEMS-tunable dielectric metasurface lens," *Nat. Commun.* **9**(1), 812 (2018).
7. C. Wang, S. Liu, Y. Sun, X. Tao, P. Sun, J. Zhang, C. Tao, R. Wu, F. Wu, and Z. Zheng, "Tunable beam splitter using bilayer geometric metasurfaces in the visible spectrum," *Opt. Express* **28**(19), 28672–28685 (2020).
8. F. Balli, M. A. Sultan, and J. T. Hastings, "Rotationally tunable varifocal 3D metalens," *Opt. Lett.* **46**(15), 3548–3551 (2021).
9. L. W. Alvarez, "Two-element variable-power spherical lens," U. S. Patent **3305294**, 350–423 (1967).

10. Z. Han, S. Colburn, A. Majumdar, and K. F. Böhringer, "MEMS-actuated metasurface Alvarez lens," *Microsyst. Nanoeng.* **6**(1), 79 (2020).
11. S. Colburn, A. Zhan, and A. Majumdar, "Varifocal zoom imaging with large area focal length adjustable metalenses," *Optica* **5**(7), 825–831 (2018).
12. L. Chen, Y. Hao, L. Zhao, R. Wu, Y. Liu, Z. Wei, N. Xu, Z. Li, and H. Liu, "Multifunctional metalens generation using bilayer all-dielectric metasurfaces," *Opt. Express* **29**(6), 9332–9345 (2021).
13. I. M. Barton, S. N. Dixit, L. J. Summers, C. A. Thompson, K. Avicola, and J. Wilhelmsen, "Diffractive Alvarez lens," *Opt. Lett.* **25**(1), 1–3 (2000).
14. J. P. B. Mueller, N. A. Rubin, R. C. Devlin, B. Croever, and F. Capasso, "Metasurface polarization optics: independent phase control of arbitrary orthogonal states of polarization," *Phys. Rev. Lett.* **118**(11), 113901 (2017).
15. R. Lin and X. Li, "Multifocal metalens based on multilayer Pancharanam-Berry phase elements architecture," *Opt. Lett.* **44**(11), 2819–2822 (2019).
16. B. Wang, Y. Dong, H. Feng, D. Yang, Z. Song, L. Xu, W. Chu, Q. Gong, and Y. Li, "Rochon-prism-like planar circular polarized beam splitters based on dielectric metasurfaces," *ACS Photonics* **5**(5), 1660–1664 (2018).
17. D. Zhang, M. Ren, W. Wu, N. Gao, X. Yu, W. Cai, X. Zhang, and J. Xu, "Nanoscale beam splitters based on gradient metasurfaces," *Opt. Lett.* **43**(2), 267–270 (2018).
18. S. Bernet and M. Ritsch-Marte, "Adjustable refractive power from diffractive Moiré elements," *Appl. Opt.* **47**(21), 3722–3730 (2008).
19. K. Iwami, C. Ogawa, T. Nagase, and S. Ikezawa, "Demonstration of focal length tuning by rotational varifocal moiré metalens in an ir-A wavelength," *Opt. Express* **28**(24), 35602–35614 (2020).
20. C. Wang, Y. Sun, Q. Zhang, Z. Yu, C. Tao, J. Zhang, F. Wu, R. Wu, and Z. Zheng, "Continuous-zoom bifocal metalens by mutual motion of cascaded bilayer metasurfaces in the visible," *Opt. Express* **29**(17), 26569–26585 (2021).
21. C. Chen, W. Song, J. Wang, Y. H. Chen, B. Xu, M. Chen, H. Li, B. Fang, J. Chen, H. Y. Kuo, S. Wang, D. P. Tsai, S. Zhu, and T. Li, "Spectral tomographic imaging with aplanatic metalens," *Light Sci. Appl.* **8**(1), 99 (2019).
22. B. H. Chen, P. C. Wu, V. Su, Y. Lai, C. H. Chu, I. C. Lee, J. Chen, Y. H. Chen, Y. Lan, C. Kuan, and D. P. Tsai, "GaN metalens for pixel-level full-color routing at visible light," *Nano. Lett.* 7b03135 (to be published).
23. H. Pahlevaninezhad, M. Khorasaninejad, Y. Huang, Z. Shi, L. P. Hariri, D. C. Adams, A. Zhu, C. Qiu, F. Capasso, and M. J. Suter, "Nano-optic endoscope for high-resolution optical coherence tomography in vivo," *Nature Photon.* **12**(9), 540–547 (2018).
24. X. Zhang, C. Guan, K. Wang, L. Cheng, J. Yang, J. Shi, H. Liu, Z. Liu, and L. Yuan, "Multi-focus optical fiber lens based on all-dielectric metasurface," *Chin. Opt. Lett.* **19**(5), 050601 (2021).
25. C. Fan, C. Lin, and G. Su, "Ultrawide-angle and high-efficiency metalens in hexagonal arrangement," *Sci. Rep.* **10**(1), 15677 (2020).
26. A. Martins, K. Li, J. Li, H. Liang, D. Conteduca, B. V. Borges, T. F. Krauss, and E. R. Martins, "On Metalenses with Arbitrarily Wide Field of view," *ACS Photonics* **7**(8), 2073–2079 (2020).
27. M. Pu, X. Li, Y. Guo, X. Ma, and X. Luo, "Nanoapertures with ordered rotations: symmetry transformation and wide-angle flat lensing," *Opt. Express* **25**(25), 31471–31477 (2017).
28. J. Zhang, J. Zeng, Y. Liu, Y. Dong, and J. Wang, "Fundamental challenges induced by phase modulation inaccuracy and optimization guidelines of geometric phase metasurfaces with broken rotation symmetry," *Opt. Express* **29**(21), 34314–34326 (2021).